RSC Advances

ROYAL SOCIETY OF CHEMISTRY

PAPER

View Article Online
View Journal | View Issue

Check for updates

Cite this: *RSC Adv.*, 2023, **13**, 23320

Enhanced removal of toxic Cr(VI) and Pb(II) from water using carboxylic terminated $Ti_3C_2T_x$ nanosheets†

Saleem Shah,[a] Iqra Mubeen,[a] Erum Pervaiz *[a] and Habib Nasir[b]

The discharge of Cr(VI)and Pb(II) contaminants into water resources through industrial waste induces a considerable risk to human and marine life, *which demands an effective removal of these toxic metal ions (MI) from the aquatic* environment. This study presents a remarkable adsorption performance of the carboxylic terminated $Ti_3C_2T_x$ nanosheets synthesized using ammonium bifluoride and citric acid and applied as adsorbents for the removal of Cr(VI)and Pb(II) from water. Adsorption efficiency was evaluated under sonication, MI concentration, and solution temperature at pH 5.5. Maximum adsorption capacities of 1090 mg g^{-1} and 1135 mg g^{-1} for Cr(VI) and Pb(II) were attained within 7 and 4 minutes, respectively. Moreover, adsorption kinetic and isotherm studies were conducted, and the experimental data was found to fit well with pseudo-second-order reaction and Freundlich models. It was also established that the main interactions to drive the adsorption reactions were the electrostatic forces between the adsorbates and $Ti_3C_2T_x$ adsorbent. Furthermore, (–COOH) and (–OH) terminal groups were the main contributors to the adsorption of Cr(VI) and Pb(II) pollutants through an ion exchange mechanism. Besides the ion exchange mechanism, chemical coordination, entrapment of the adsorbates, and van der Waals forces lead to a physiochemical interaction between the MI and $Ti_3C_2T_x$ nanosheets. In addition, $Ti_3C_2T_x$ nanosheets showed better selectivity towards Pb(II) removal than Cr(VI) in an aqueous solution. The nanosheets also exhibited more than 80% removal efficiency even after six cycles of regeneration and reusability. Additionally, $Ti_3C_2T_x$ nanosheets offered superior adsorption performance for Cr(VI) and Pb(II) compared to previously reported titanium carbide MXenes and activated carbon-based adsorbents. Hence, these high-quality and efficient $Ti_3C_2T_x$ nanosheets can potentially eradicate other hazardous MI contaminants from wastewater.

Received 23rd May 2023
Accepted 24th July 2023

DOI: 10.1039/d3ra03456a

rsc.li/rsc-advances

1. Introduction

The discharge of heavy metal (HM) contaminants into potable and wastewater through industrial waste has raised global concern.[1,2] Cr and Pb[3] are listed among the top five HM ions which induce human poisoning.[4] Cr exists in trivalent and hexavalent ion states as Cr(III) and Cr(VI), respectively. Intake of Cr(VI) is highly poisonous to organs and often leads to asthma and lung cancer.[5] Likewise, Pb(II) at high concentrations can cause damage to gastrointestinal, renal and cardiovascular systems.[6,7] So, water treatment for eradicating MI has gained immense attention.[8] Different protocols[9] as elaborated by Tawfik A. Saleh are practiced for the synthesis of adsorbents to extract the pollutants from water. In addition, current techniques, which include flocculation,[10] adsorption,[11] ion exchange,[12] solvent extraction,[13] chemical precipitation,[14] membrane filtration,[15] electrochemical treatment[16] and reverse osmosis[17] are adopted for water treatment. However, adsorption is considered a superior technique for its simplicity, and easy availability of the adsorbent materials.[18,19] Agricultural waste,[20] zeolites,[21] clay minerals,[22] biopolymers,[3] and activated carbon[20] are the conventional adsorbents being used. Since electrostatic interactions favour the adsorption of Cr(VI)[23] and Pb(II)[24] in aqueous media, therefore, adsorbents like Ti_3CT_x MXenes with negatively charged surfaces demonstrate better adsorption capacity for the cationic pollutants. Although, Cr(VI) ions exist either in the form of CrO_4^{2-} or $Cr_2O_7^{2-}$ in water, yet these ions interact with the H^+ of the (–OH) groups, and meanwhile, electrons transfer from the MXene to Cr(VI), which further reduce it to Cr(III) as reported by Ying *et al.*[25] Thus, the reduction of Cr(VI) to Cr(III), and its adsorption onto Ti–O on the surface of MXene nanosheets occurs simultaneously.

$Ti_3C_2T_x$ MXenes are two-dimensional (2D) nanosheets, which possess active sites in the form of terminal functional groups. This makes the nanosheets more viable for the

---

[a] *School of Chemical and Materials Engineering, National University of Sciences and Technology, Sector H12, Islamabad 44000, Pakistan. E-mail: erum.pervaiz@student.nust.edu.pk*

[b] *School of Natural Sciences, National University of Sciences and Technology, Sector H12, Islamabad 44000, Pakistan*

† Electronic supplementary information (ESI) available. See DOI: https://doi.org/10.1039/d3ra03456a

adsorption of metal pollutants than the other 2D adsorbents.[26] Due to the large specific surface area (SSA), hydrophilicity, and chemical stability, the nanosheets show better removal performance for Cr(VI)[27,28] and Pb(II)[29,30] in water. Numerous researchers have synthesized Ti_3C2T_x MXenes grafted with (–OH),[31] and (=O) terminations and applied these nanosheets for the removal of pollutants from the aquatic environment. For instance, Ying *et al.* synthesized $Ti_3C_2T_x$ nanosheets, which displayed a 250 mg g^{-1} removal capacity for Cr(VI).[32] Perumal Karthikeyan and coworkers studied $Ti_3C_2T_x$ nanosheets to remove Cr(VI)[33] and achieved an adsorption capacity of 104 mg g^{-1}. They also confirmed chemisorption as a driving mechanism in the uptake of pollutant ions. Wang et al. synthesized a nanocomposite material by integrating Ti_3C2T_x nanosheets and TiO_2 nanoparticles using a hydrothermal method.[34] Their objective was to develop a nanomaterial composite with abundant active sites, which showed three times greater adsorption performance for Cr(VI) than that of pristine titanium carbide. Similarly, $Ti_3C_2T_x$ nanosheets displayed a high adsorption potential for Pb(II) contaminant. Peng *et al.* presented a preferential Pb(II) adsorption behaviour of the MXenes nanosheets.[35] They suggested that (–OH) terminal functional groups provided the sites for adsorption through an ion exchange mechanism. Shuhao Wang and teammates functionalized $Ti_3C_2T_x$ MXenes using bio-surfactants such as lignosulfonate, enzymatic hydrolysis lignin, and chitosan.[36] Thus, the adsorption capacity of the MXenes for Pb(II) removal was enhanced to 233 mg g^{-1} by augmenting the existing active sites of the nanosheets. Furthermore, $Ti_3C_2T_x$ was modified using a silane coupling agent (KH570), which displayed better adsorption performance for Pb(II).[29] The terminal function groups of $Ti_3C_2T_x$ MXenes play a vital role in the adsorption of the cationic pollutants. Therefore, investigations are being conducted to further improve the adsorption performance of the nanosheets by augmenting the surface terminations with other functional groups. However, to the best of our knowledge, no study in terms of the synthesis and application of the of carboxylic terminated $Ti_3C_2T_x$ nanosheets, especially for the removal of toxic Cr(VI) and Pb(II) contaminates from an aqueous media has been presented to date.

In this work, the synthesis of (–COOH) embedded $Ti_3C_2T_x$ nanosheets using citric acid and their further application for the removal of Cr(VI) and Pb(II) from water is demonstrated successfully. The main objective of the study is to evaluate and optimize the adsorption performance of the nanosheets for the effective removal of the MI pollutants from water. In addition, the adsorption experiments are conducted under the influence of various concentrations of MI, sonication duration, and solution temperatures at a constant pH. Pre and post-metal-adsorbed nanosheets are analyzed using XRD, FTIR, XPS, SEM, TEM, BET, EDX, and AAS techniques. Moreover, adsorption kinetics and isotherms studies are incorporated, and it is established that $Ti_3C_2T_x$ nanosheets embedded with (–COOH) surface terminations offer an extraordinary and superior adsorption performance for Cr(VI) and Pb(II), compared to the previously reported $Ti_3C_2T_x$ adsorbents. Finally, the selectivity of the nanosheets towards metal pollutants, and the regeneration and reusability of the adsorbent over several cycles are also investigated for further practical applications.

2. Materials and methods

2.1 Chemicals

Ti_3AlC_2 MAX phase powder of 200-mesh particle size and ammonium bifluoride (NH_4HF_2) were procured from Shanghai Macklin, China. Citric acid monohydrate ($C_6H_8O_7 \cdot H_2O$) and lead nitrate ($Pb(NO_3)_2$) were obtained from Merck, USA. Tetramethylammonium hydroxide (TMAOH), 25 weight% in methanol, was purchased from Acros, USA. Potassium dichromate ($K_2Cr_2O_7$), sodium hydroxide (Na(OH)), and hydrogen chloride (HCl) were acquired from Sigma Aldrich, USA. All chemicals purchased and used were of analytical grades.

2.2 Synthesis of $Ti_3C_2T_x$ nanosheets

$Ti_3C_2T_x$ Nanosheets were synthesized through wet chemical etching of Ti_3AlC_2 MAX phase. Five major steps: etching, centrifugation, delamination, vacuum filtration and drying were adopted to obtain the nanosheets. The synthesis protocol commenced with the preparation of an etching solution. 100 mL and 200 mL solutions of DI water containing 7.3 g NH_4HF_2, and 5 g citric acid, respectively, were prepared separately. The solutions were then mixed in a plastic container, and 4 g Ti_3AlC_2 powders were gradually immersed into it. The reaction was set at room temperature (23 ± 2 °C) for a continuous stirring at 750 rpm for 72 hours (h) using a Teflon stirrer and magnetic plate. The lid of the container was loosely closed to ensure the escape of H_2 gas generated during the etching reaction. After completing the first step, the obtained suspension containing residual citric acid, HF acid and salts contents was washed through five cycles of centrifugation at 4500 rpm using deionized (DI) water, and each cycle lasted for 30 minutes (min). On the termination of last cycles, the solution's pH was checked and found to be 5.5. Then, the supernatant was decanted and the slurry was retained for further treatment. The next step was to intercalate and delaminate the obtained wet sediment of multilayered $Ti_3C_2T_x$ nanosheets. The sediment was added to a 300 mL solution containing 4 mL TMAOH and 296 mL DI water, and stirring was performed at 750 rpm for 72 h. Then, the ultrasonic bath sonication of the suspension was carried out at 30 kHz (45 °C) for 3 h. Subsequently, a thick black colloidal solution was obtained. To wash out the intercalated TMAOH contents, the solution was centrifuged for three cycles, and each cycle was run at 3500 rpm for 10 min. Then, the vacuum filtration of the solution was conducted using a 0.45 μm pores size hydrophilic membrane (PVDF). The extracted slurry was rinsed with 2000 mL DI water to remove the leftover traces of TMAOH. Finally, the MXenes paste was vacuum-dried at 90 °C for 60 h. Resultantly, 3.55 g $Ti_3C_2T_x$ nanosheets powders were obtained.

2.3 Adsorption procedure

The adsorption study was performed using a batch method, and the protocol commenced with the preparation of synthetic wastewater containing targeted pollutants. A 600 mL stock solution containing Cr(VI) adsorbate *i.e.*, 200 ppm $K_2Cr_2O_7$ in DI water was prepared in an Erlenmeyer flask. Then, 300 mg of $Ti_3C_2T_x$ nanosheets (adsorbent) were immersed into the solution, and kept it in a thermostatic shaking bath at 250 rpm and room temperature for 72 h. Likewise, a stock solution containing Pb(II) adsorbate *i.e.* $Pb(NO_3)_2$, was prepared following the same parameters and doses of the salt and adsorbent as in the case of Cr(VI). So, two stock solutions containing Cr(VI) and Pb(II) loaded $Ti_3C_2T_x$ nanosheets were prepared, and called batch-1 solutions. The solutions' pH was brought to 5.5 by adding 0.1 M HCl and 0.1 M NaOH.[26,32] Moreover, the above protocol was repeated for the preparation of subsequent four stock solutions of the higher doses of Cr(VI) and Pb(II), which were of 400 ppm, called batch-2, and 600 ppm, called batch-3. Thus, overall six stock solutions of 200 ppm, 400 ppm, and 600 ppm concentrations of the Cr(VI) and Pb(II) adsorbates were prepared separately. After that, nine sample solutions from each stock solution were extracted and subjected to the effects of sonication at 30 kHz for 10 min, 20 min and 30 min, and temperatures at 25 °C, 50 °C and 75 °C. The detail of these samples as extracted from 200 ppm stock solution is also is summarized in Table S1 (ESI†) for better assimilation. Moreover, to know the equilibrium concentration and time, and to conduct kinetics and isotherm studies, aliquots of 10 mL from each sample solution was collected with a regular interval of 2 min, which was further vacuum filtered using a 0.45 μm pores size PVDF membrane. MI containing solutions separated *via* filtration were taken in vials and labelled for further analysis to determine the residue concentration of the pollutants. In addition, the obtained paste of MI loaded $Ti_3C_2T_x$ was vacuum-dried at 50 °C for 24 h to remove the water content. The dried Cr(VI) and Pb(II) loaded $Ti_3C_2T_x$ nanosheets powders were termed Cr–$Ti_3C_2T_x$ and Pb–$Ti_3C_2T_x$, respectively.

In addition, the adsorption capacities and selectivity of $Ti_3C_2T_x$ nanosheets towards Cr(VI) and Pb(II) in a combined feed solution (containing both pollutants) were evaluated. Therefore, a 200 mL solution containing 400 ppm concentration of each co-ion and 100 mg MXenes powder was prepared at pH 5.5. The solution was further stirred for 72 h. Likewise, to analyze the adsorption capacities of the nanosheets towards the same targeted pollutants in the presence of other competing ions, two separate solutions were prepared: one solution contained 200 mL DI water and 100 ppm concentration of Cr(VI), and similarly, the other solution contained Pb(II). Then, both solutions were fed with 100 ppm each of Ca(II), Na(II) and K(I), and immersed with 100 mg MXenes powder under a constant pH of 5.5, and stirred for 72 h. Subsequently, vacuum filtration of those three solutions was performed to obtain the filtrate and assess the residue concentration of each MI.

2.4 Characterizations

X-ray diffraction (XRD) (PANalytical) was utilized to examine the crystallinity and structure of synthesized $Ti_3C_2T_x$ nanosheets and Cr–$Ti_3C_2T_x$ and Pb–$Ti_3C_2T_x$ samples. Terminal groups of the MXenes nanosheets were evaluated *via* Fourier-transform infrared spectroscopy (FTIR) (JASCO-460 plus FTIR spectrometer, Japan). Chemical composition, surface Chemistry and adsorption mechanism of the pristine and metal adsorbed nanosheets were investigated using X-ray photoelectron spectroscopy (XPS) (PHI Quantera SXM; ULVAC-PHI, Japan). The morphology of the samples was analyzed using a transmission electron microscope (TEM) (JEM 1400Flash, JEOL, Japan) and scanning electrons microscope (SEM) (JSM-6490A, JEOL, Japan). The SSA of the MXenes samples was evaluated using Brunauer–Emmett–Teller (BET) (Quantachrome NovaWin-NOVA). Energy dispersive X-ray (EDX) (EDAX Z2-i7 analyzer Bruker, Germany) was applied to find the elemental composition of the MXenes samples. Atomic adsorption spectrophotometry (AAS) (Analytika-Jena Nova 800, Germany) was applied to assess the residue concentrations of the MI in the solutions.

3. Results and discussion

3.1 Structure and surface chemistry

XRD spectrums were recorded to study the structure of synthesized and adsorbates-loaded $Ti_3C_2T_x$ nanosheets. Fig. 1(a) shows XRD patterns of Ti_3AlC_2 MAX phase, $Ti_3C_2T_x$ adsorbent, Cr–$Ti_3C_2T_x$, and Pb–$Ti_3C_2T_x$ nanosheets, which correspond to JCPDS # 00-052-0875, 00-051-0622, 01-089-2726 and 01-071-0298, respectively. The elimination and shifting of peaks attributed to (002), (004), (101), (104), and (105) lattice planes of Ti_3AlC_2 and the subsequent emergence of new broad peaks in $Ti_3C_2T_x$ nanosheets spectrum confirm the successful exfoliation of the MAX phase. These diffraction peaks in the MXenes pattern are observed due to the replacement of Al atoms of Ti_3AlC_2 by (–COOH), (–OH), (=O), and (–F) terminal functional groups.[31,37] Furthermore, the downward shift of the peak at 2θ angle of 9.49° in the MAX phase to 7.06° in the MXenes pattern corresponds to an increment in lattice parameters (c), which validates the intercalation and delamination of $Ti_3C_2T_x$ nanosheets. However, the diffraction peak at 2θ angle of 7.06° in $Ti_3C_2T_x$ MXenes shifts upward to 7.12° and 7.16° in Cr–$Ti_3C_2T_x$ and Pb–$Ti_3C_2T_x$ samples, respectively. This indicates that d-spacing decreases in MXenes nanosheets due to the adsorption of metal cations. Which reduces the repulsive force between negatively charged terminal groups on MXenes nanosheets and increases the thickness of the sheets accordingly. In addition, the greater 2θ angle at 7.16° in the Pb–$Ti_3C_2T_x$ spectrum reflects more uptake of Pb(II) than Cr(VI) by nanosheets adsorbent. Furthermore, the diffraction peaks in Cr–$Ti_3C_2T_x$ and Pb–$Ti_3C_2T_x$ spectrums display relatively lower intensities than $Ti_3C_2T_x$ nanosheets. This implies an alteration in the lattice planes of the nanosheets due to MI adsorption. Likewise, the diffraction peak at 2θ angle of 14.20° in the $Ti_3C_2T_x$ nanosheets spectrum can also be noticed in the Cr–$Ti_3C_2T_x$ spectrum but with lesser intensity. In contrast, the same peak entirely disappears in the spectrum of Pb–$Ti_3C_2T_x$ samples, which reflects more Pb(II) is adsorbed by the adsorbent.

FTIR analysis was performed to find the nature and driving interactions of the terminal functional groups on $Ti_3C_2T_x$ nanosheets. Fig. 1(b) shows infrared spectrums of Ti_3AlC_2 MAX phase, bare and metal-loaded $Ti_3C_2T_x$ nanosheets. The characteristic peaks at 3423 cm^{-1}, 2915 cm^{-1}, 1633 cm^{-1}, 1357 cm^{-1}, 1050 cm^{-1}, and 585 cm^{-1} correspond to O–H, C–H, C=O, C–O,

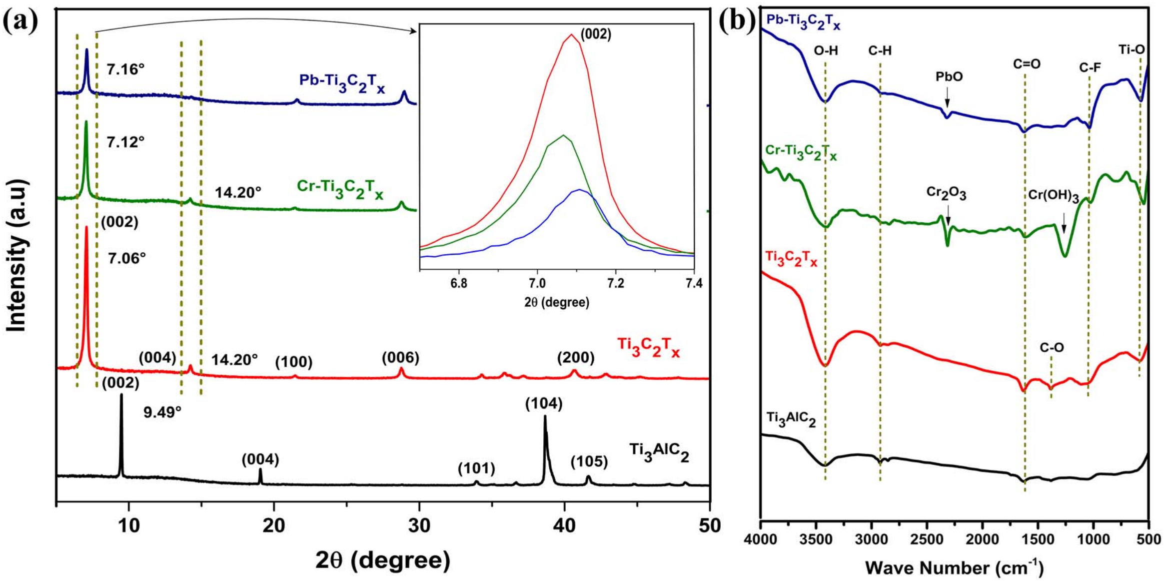

Fig. 1 (a) XRD patterns of Ti_3AlC_2 MAX phase, bare and MI loaded $Ti_3C_2T_x$ nanosheets, and the zoomed-in image at the top right corner to show the post adsorption shifting of 2θ angle at ~7° (the underneath hidden spectrums at range of 2θ angle at ~30°–50° have same structure as of $Ti_3C_2T_x$), and (b) FTIR spectrums of Ti_3AlC_2 MAX phase, bare and MI loaded $Ti_3C_2T_x$ nanosheets.

C–F, and Ti–O stretching vibrations, respectively represent the $Ti_3C_2T_x$ nanosheets. Here, the C–H band is attributed to aliphatic stretching vibration and C═O, and C–O bands are assigned to the stretching of carboxylic groups.[38] This further confirms the embedding of (–OH), (═O), (–COOH), and[31] terminal functional groups onto $Ti_3C_2T_x$ nanosheets in the etching process. In addition, the broader and weaker peak in the MAX phase spectrum corresponds to O–H stretching vibrations, which denote the moist contents. However, the same peak in the spectrum of $Ti_3C_2T_x$ nanosheets is relatively more intense due to the presence of (–OH) terminations. The adsorption of MI by $Ti_3C_2T_x$ nanosheets is reflected by observing a decline in the intensities of peaks in Cr–$Ti_3C_2T_x$ and Pb–$Ti_3C_2T_x$ spectrums. The Cr(VI) and Pb(II) loaded nanosheets display an additional peak at 2315 cm^{-1}, attributed to Cr_2O_3 and PbO at C≡C stretching vibration. In addition, a strong peak at 1260 cm^{-1} can be noticed in Cr–$Ti_3C_2T_x$, attributed to $Cr(OH)_3$,[39] which reflects a reduction of the Cr(VI) to Cr(III) state during the adsorption process. However, during this process Ti–C active layer of the MXene is partially oxidized into TiO_2, which decreases the stability and dispersity of the MXenes nanosheets in an aqueous media. Resultantly, the regeneration of Cr(VI) loaded $Ti_3C_2T_x$ is less effective as compared to Pb(II) loaded MXenes.

XPS technique was used to analyze the composition, surface chemistry, and adsorption mechanism of the $Ti_3C_2T_x$ nanosheets. Fig. 2(a) shows a survey scan of the bare and MI loaded nanosheets, which indicates the characteristics peaks of Ti, C, O, F, Cr, and Pb elements in the respective spectra. The bonding state of the Ti 2p is shown in Fig. 2(b), which reflects the formation of titanium-containing terminals as well as titanium carbides (T–OH, T═O, T–C).[40,41] Furthermore, Fig. 2(c) displays the bonding state of O 1s, which reveals three peaks at 528.1 eV, 530.3 eV, and 531.8 eV attributed to the (–OH) groups of $Ti_3C_2T_x$, the O of the TiO_2, and the C═O of the carboxylic group, respectively.[42] Likewise, Fig. 2(d) shows the bonding state of C 1s, which confirms the bonds between carbon and oxygen (O═C–O, C–O–C) *vis-a-vis* graphite (C–C) and carbide (C≡C) like bonds. However, a drop in the intensities of peaks at 281.9 eV, 284.9 eV, 287.6 eV, and 289.3 eV implies the breaking of the respective bonds during the adsorption process and a decrease in the active sites or terminal functional groups. Hence, the overall etching of Al atoms from the precursor MAX phase and the subsequent grafting of terminal groups, including (–COOH) onto $Ti_3C_2T_x$ nanosheets, is established. In addition, the XPS patterns of MI loaded $Ti_3C_2T_x$ reveal the satellite bands of the well-adsorbed Cr(VI) and Pb(II) adsorbates.[26,32]

SEM and TEM images in Fig. S1 (ESI†) display the morphology of Ti_3AlC_2, $Ti_3C_2T_x$ MXenes, Cr–$Ti_3C_2T_x$, and Pb–$Ti_3C_2T_x$ nanosheets. The MAX phase presents a well-compact layered structure, whereas $Ti_3C_2T_x$ MXenes show a lamella-like structure, which reveals a successful exfoliation of Ti_3AlC_2 into 2D nanosheets. Hence, $Ti_3C_2T_x$ nanosheets offer a large SSA and more active sites for the adsorption of Cr(VI) and Pb(II) adsorbates. In contrast to $Ti_3C_2T_x$ nanosheets, compressed sheets of Cr–$Ti_3C_2T_x$ and Pb–$Ti_3C_2T_x$ can be noticed due to the accumulation of Cr(VI) and Pb(II) adsorbates, which reflects a decrease in the SSA of the nanosheets. This finding is also confirmed through BET analysis. The SSA of the bare $Ti_3C_2T_x$ MXenes was evaluated as 42.63 m^2 g^{-1}, whereas after adsorption, it decreased to 26.13 m^2 g^{-1} and 18.35 m^2 g^{-1} for Cr(VI) and Pb(II) loaded MXenes, respectively. N_2 adsorption–desorption isotherms indicate a significant decrease in the SSA of MXenes nanosheets after MI adsorption, as shown in Fig. S2 (ESI†). Moreover, the TEM images of the $Ti_3C_2T_x$ nanosheets show ~4.76 nm thick but well-expanded flakes due to repulsive forces between the negatively charged nanosheets. However, an apparent

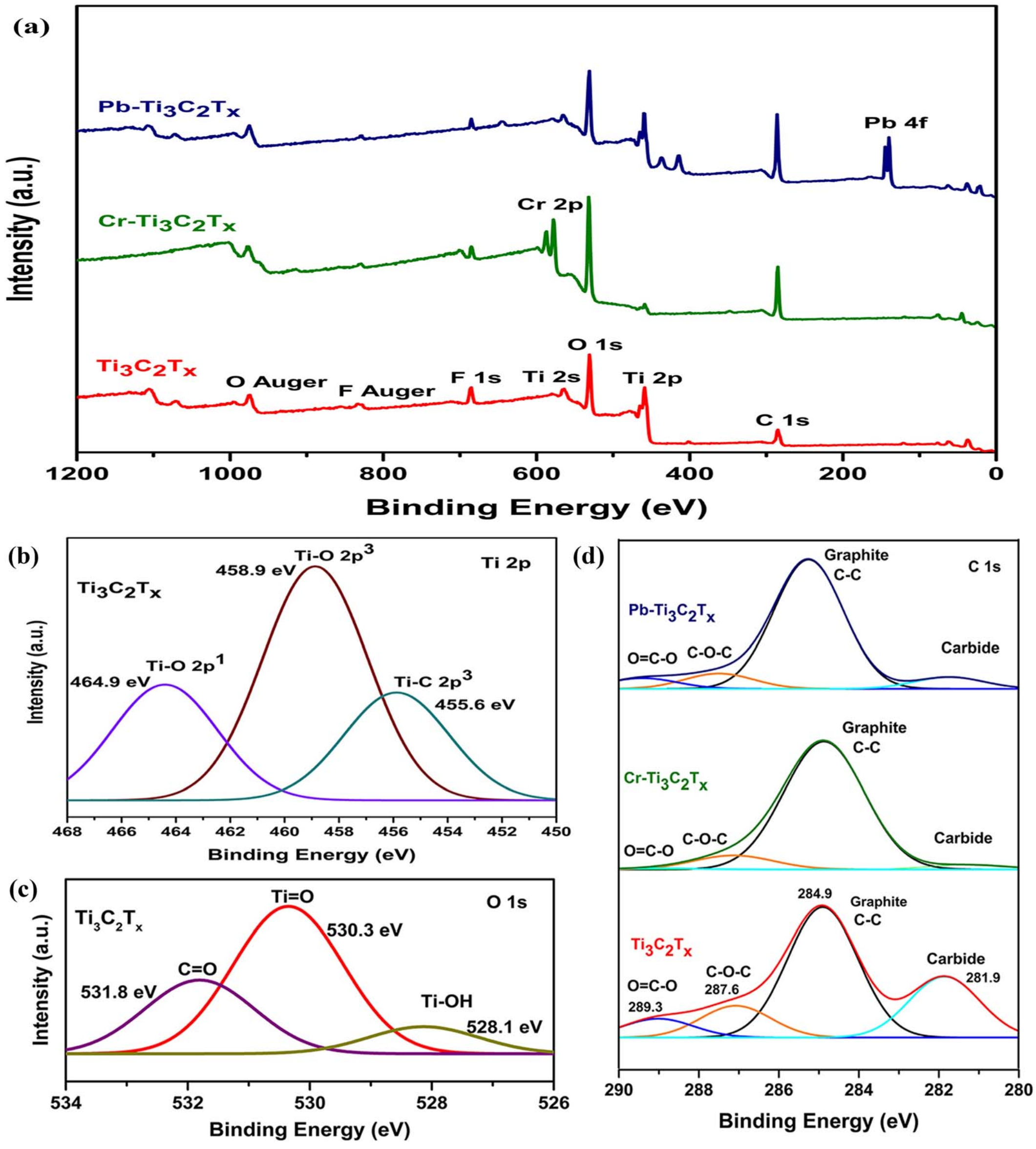

Fig. 2 The XPS spectrums of (a) a wide-scan of the pre and post-adsorption $Ti_3C_2T_x$ nanosheets, (b) Ti 2p, (c) O 1s bonding states of the $Ti_3C_2T_x$ nanosheets, and (d) C 1s bonding states of the bare and MI loaded $Ti_3C_2T_x$ nanosheets.

decrease in *d*-spacing and an increase in sheet thickness can be observed in the adsorbates-loaded nanosheets. EDX results also support the findings drawn from the SEM and TEM analysis. EDX data given in Table S2 (ESI†) and its spectrums, as displayed in Fig. S3 (ESI†), illustrate the elemental composition of the samples. Ti_3AlC_2 MAX phase contains Ti, C, and Al atoms only, and $Ti_3C_2T_x$ nanosheets comprise Ti, C, O, N, and F atoms. This indicates the etching of Al atoms and the subsequent attachment of terminal functional groups to the MXenes nanosheets. Moreover, the composition of Cr–$Ti_3C_2T_x$ and Pb–$Ti_3C_2T_x$ samples confirms the uptake of MI.

3.2 Adsorption performance

The adsorption performance of $Ti_3C_2T_x$ nanosheets was evaluated under various parameters, including sonication, MI dosage, and solution temperature at pH 5.5, using eqn (1) and (2). The impact of these parameters on adsorption performance of the nanosheets has been further discussed in the succeeding sub-sections. However, AAS was applied to assess the residue concentrations of Cr(VI) and Pb(II) in the aqueous solutions. Hence, the maximum adsorption capacities of 1090 mg g^{-1} and 1135 mg g^{-1} for Cr(VI) and Pb(II), respectively, are plotted in Fig. 3. In addition, the weight of Cr(VI) and Pb(II) loaded $Ti_3C_2T_x$ MXenes powder, even after vacuum drying was found increased up to 109% and 113%, respectively, as compared to the bare MXenes. Furthermore, the adsorption capacities of the previously reported $Ti_3C_2T_x$ nanosheets and activated carbon are comparatively summarized in Table 1.

$$\text{Adsorption capacity}\ \left(\text{mg g}^{-1}\right) = \frac{(C_\text{o} - C_t)}{M} \times V \qquad (1)$$

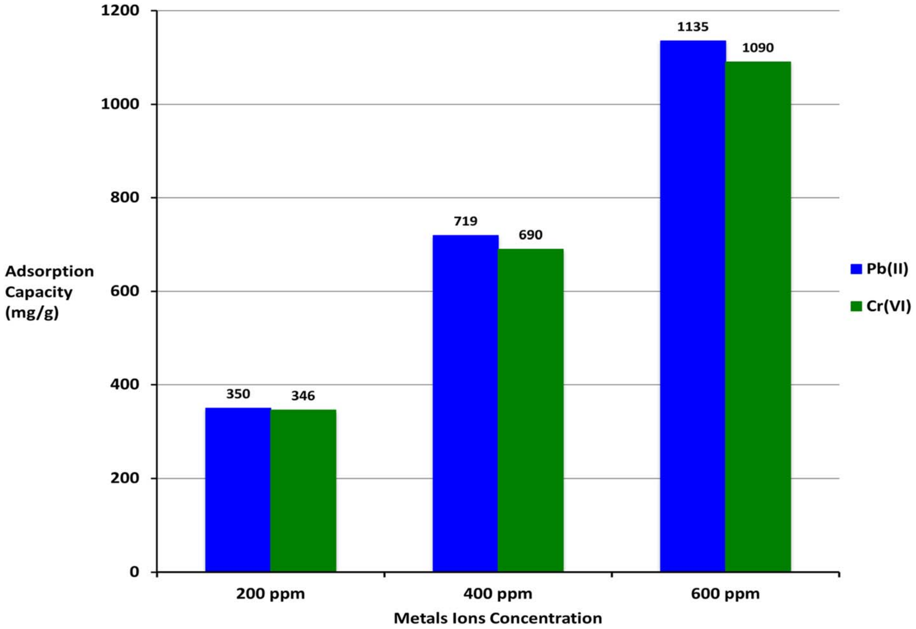

Fig. 3 The adsorption capacities of $Ti_3C_2T_x$ nanosheets for Cr(VI) and Pb(II) adsorbates at 200 ppm, 400 ppm and 600 ppm concentrations in an aqueous media.

$$\text{Adsorption efficiency } (\%) = \frac{(C_o - C_t)}{C_o} \times 100 \qquad (2)$$

where C_o represents the initial concentration, and C_t indicates the residual concentration of MI (mg per litre) at a specific time. V is the volume of solution (litre), and M is the mass of the MXenes powders (gram).

3.2.1 Effect of sonication. The influence of sonication at 30 kHz for 10 min, 20 min, and 30 min span on the adsorption capacity of $Ti_3C_2T_x$ nanosheets was analyzed. As presented in

Table 1 Presents the comparative adsorption capacities of various $Ti_3C_2T_x$ and activated carbon based adsorbents for Cr(VI) and Pb(II) contaminants in the aqueous environment

Sr #	MXenes	MI	Adsorption capacity (mg g^{-1})	Reference
1	$Ti_3C_2T_x$	Pb(II)	1135	This study
2	$Ti_3C_2T_x$	Pb(II)	36.60	43
3	AlkMXene-NH_2	Pb(II)	384.63	26
4	Bio surfactant functionalized $Ti_3C_2T_x$	Pb(II)	232.90	44
5	MXene/alginate nanocomposite	Pb(II)	382.7	36
6	$Ti_3C_2T_x$	Pb(II)	140	36
7	Enzymatic hydrolysis lignin functionalized Ti_2CT_x MXene	Pb(II)	232.9	35
8	$Ti_3C_2T_x$-KH570	Pb(II)	147.29	29
9	$Ti_3C_2T_x$	Pb(II)	147.97	45
10	MAX@titanate	Pb(II)	328.90	29
11	Magnetized activated carbon	Pb(II)	253.20	46
12	Mesoporous activated carbon	Pb(II)	47.17	47
13	$Ti_3C_2T_x$	Cr(VI)	1090	This study
14	NH_2–$Ti_3C_2T_x$	Cr(VI)	107.40	48
15	MXene/PEI modified sodium alginate aerogel	Cr(VI)	538.97	49
16	Ti_3C_2	Cr(VI)	80	50
17	nZVI-Alk-Ti_3C_2 composites	Cr(VI)	194.87	51
18	$Ti_3C_2T_x$ based film	Cr(VI)	84	52
19	$Ti_3C_2T_x$/PmPD-5/1	Cr(VI)	540.47	53
20	$Ti_3C_2T_x$ (u-RTC)	Cr(VI)	225	54
21	δ-MnO_2/MXene	Cr(VI)	353.87	55
22	$Ti_3C_2T_x$	Cr(VI)	250	32
23	Fe_3O_4/AC	Cr(VI)	4.4	56
24	AC-iron oxide nanocomposite	Cr(VI)	500	57

Fig. 4(a), maximum adsorption capacity is achieved in 10 min of sonication against all doses of MI. This is due to the dispersion of MXenes nanosheets through shear forces generated by cavitation bubbles in the solution medium.[58] Resultantly, more functional groups are exposed to the MI, which leads to a better interaction between the charged species. However, sonication for 20 min, as well as 30 min, exhibits no substantial influence on the adsorption performance of $Ti_3C_2T_x$ nanosheets. Instead, a minor decline in the adsorption capacity of the nanosheets at 600 ppm concentration of the MI is observed, which is due to the elevated temperature of the solution owing to sonication *i.e.*, temperature raised from ambient to ~46 °C. This further weakens the van der Waal interactions between the MI and MXenes nanosheets. However, the adsorption capacities under 200 ppm and 400 ppm at 30 min sonication do not decrease significantly, which indicates that at this level of MI dosage, most of the adsorption takes place through chemisorption due to the availability of ample active sites or surface terminations onto MXenes nanosheets.

3.2.2 Effect of MI dosage. Fig. 4(b) shows that the adsorption capacity of $Ti_3C_2T_x$ nanosheets enhances with the increased dose of MI in the aqueous solution. Initially, at a 200 ppm dose of the MI, 346 mg g^{-1} and 350 mg g^{-1} adsorption capacities are achieved. Finally, at 600 ppm, the adsorption capacities surge to 1090 mg g^{-1} and 1135 mg g^{-1}

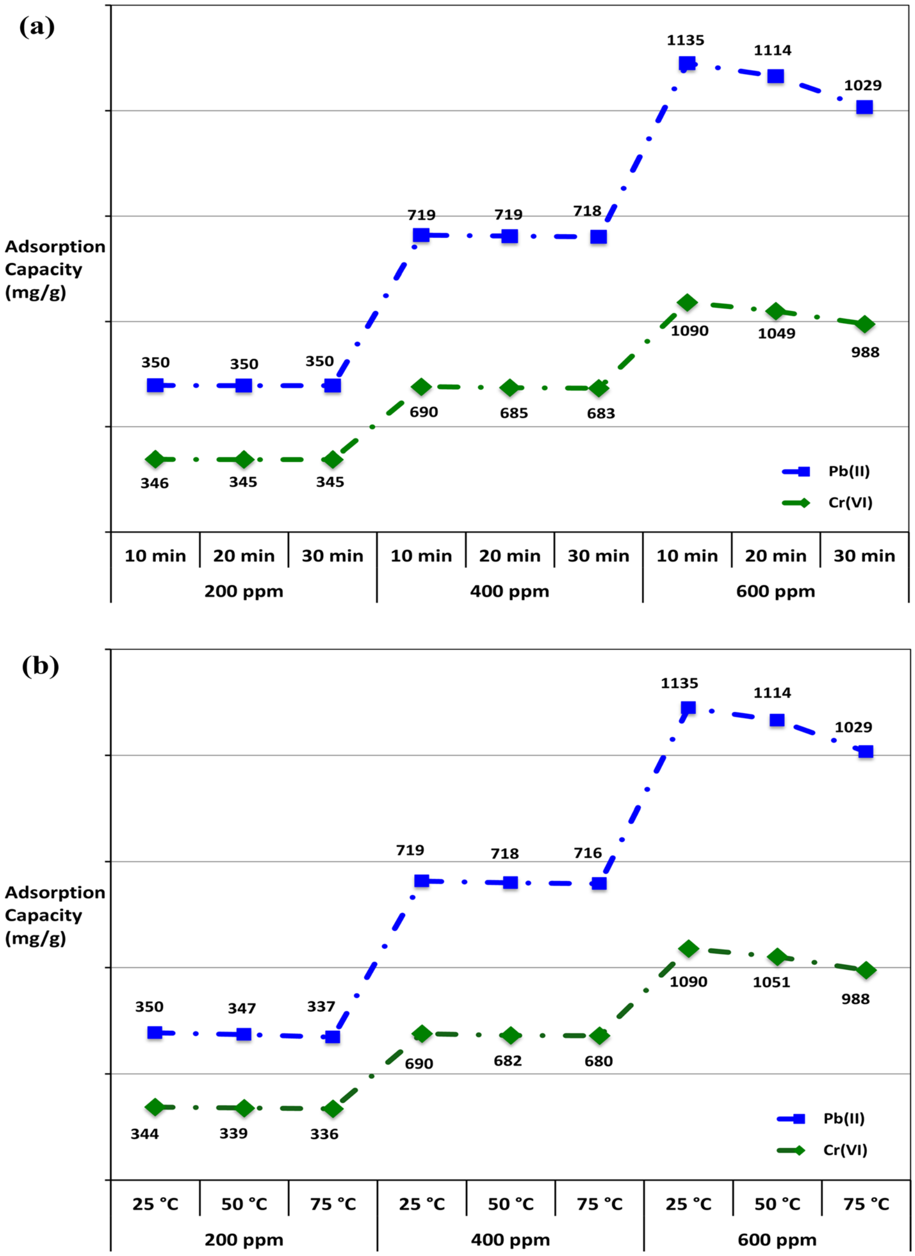

Fig. 4 The effects of (a) 30 kHz sonication for 10 min, 20 min and 30 min duration, and adsorbates dosage of 200 ppm, 400 ppm and 600 ppm, and (b) solution temperatures of 25 °C, 50 °C and 75 °C on the adsorption capacity of $Ti_3C_2T_x$ nanosheets.

for Cr(VI) and Pb(II), respectively. After that, no significant rise in the adsorption capacities of the nanosheets can be noticed, as shown in Fig. S4 (ESI†), due to the non-availability of the active sites on the adsorbent's surface.

3.2.3 Effect of solution temperature. The adsorption of Cr(VI) and Pb(II) by $Ti_3C_2T_x$ nanosheets was also analyzed at various solution temperatures. Like sonication, with an increase in temperature from 25 °C to 50 °C and 75 °C, a slight decline in the adsorption occurs, especially at the high dosage of the MI, as shown in Fig. 4(b). This is due to the weakening of van der Waal forces between the MI and nanosheets. This further reflects that the adsorption of MI by $Ti_3C_2T_x$ nanosheets is caused by chemisorption coupled with limited physisorption. Most importantly, the primary binding forces between positively charged adsorbates and negatively terminated MXenes nanosheets adsorbent operate through

Table 2 The adsorption kinetics data of the PFO and PSO reactions for Cr(VI) and Pb(II) at 25 °C, 50 °C and 75 °C temperatures

HM ion	Temperature (°C)	t_{eq} (min)	q_{exp} (mg g^{-1})	PFO k_1 (min^{-1})	PFO R^2	PSO k_2 (g mg^{-1} min^{-1})	PSO R^2
Cr(VI)	25	7	1088	0.5581	0.9736	1.4×10^{-3}	0.9908
	50	9	1049.3	0.472	0.9793	2.3×10^{-3}	0.9968
	75	11	998.64	0.2513	0.9028	2.0×10^{-3}	0.9975
Pb(II)	25	4	1131	0.8293	0.9960	3.91×10^{-3}	0.9978
	50	6	1112.66	0.7981	0.9961	4.04×10^{-3}	0.9975
	75	8	1026	0.6036	0.7836	9.0×10^{-3}	0.9998

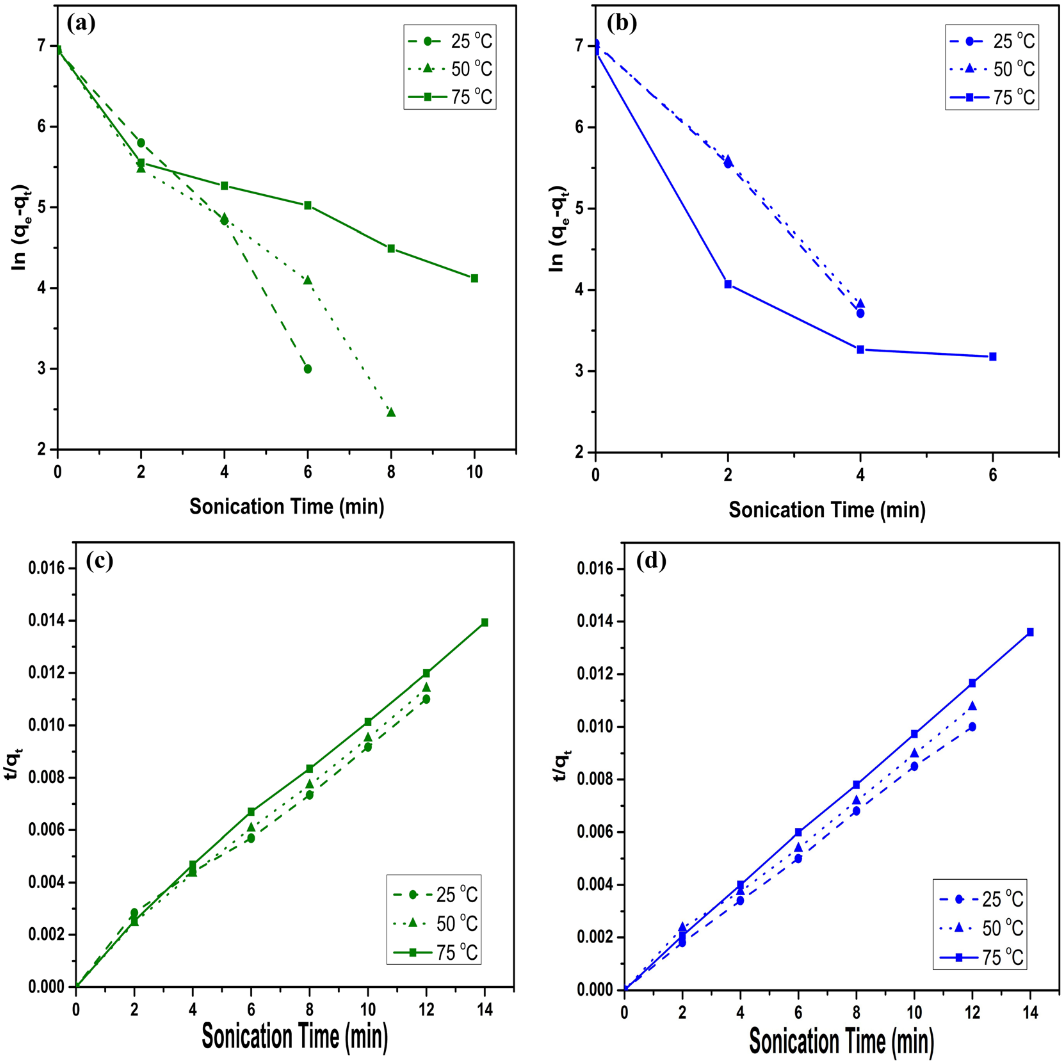

Fig. 5 PFO reaction kinetics for (a) Cr(VI) and (b) Pb(II), and PSO reaction kinetics for (c) Cr(VI) and (d) Pb(II) adsorbates at 25 °C, 50 °C and 75 °C temperatures under various duration of 30 kHz sonication.

a chemisorption process. These interactions cannot be influenced at such a range of temperatures. Hence, it implies that the migration of MI and subsequent adsorption by $Ti_3C_2T_x$ nanosheets are not temperature-dependent phenomena at 25 °C to 75 °C.

3.3 Adsorption study

The kinetic study of MI adsorbates and $Ti_3C_2T_x$ adsorbent was incorporated with pseudo-first-order (PFO) and pseudo-second-order (PSO) reactions by following eqn (3) and (4), respectively. The linear PFO and linear PSO models[59,60] were implemented for adsorption kinetics analysis. Here, q_e and q_t are the corresponding adsorption capacities (mg g^{-1}) of $Ti_3C_2T_x$ nanosheets at equilibrium and time t. Likewise, k_1 and k_2 are the respective rate constants of PFO and PSO reactions. These values are also presented in Table 2.

$$\ln(q_e - q_t) = \ln q_e - k_1 t \tag{3}$$

$$\frac{t}{q_t} = \frac{1}{k_2 {q_e}^2} + \frac{1}{q_e} t \tag{4}$$

The linear graphs of $\ln(q_e - q_t)$ *vs.* t, as shown in Fig. 5(a) and (b), and t/q_t *vs.* t, as shown in Fig. 5(c) and (d), were used to determine the respective k_1 and k_2 at 25 °C, 50 °C and 75 °C. Here, the correlation coefficient (R^2) of Cr(VI) and Pb(II) is higher for the PSO reactions than for the PFO reactions. Hence, the PSO model fits more accurately to the experimental data, which indicates that the MI are dominantly adsorbed through chemisorption reaction by the adsorbent. Whereas, condition for PSO is the rate of adsorption depends upon the adsorption capacity rather than adsorbate concentration. Hence, chemisorption coupled with a physisorption reaction on the adsorbent's surface leads to the enhanced adsorption of the adsorbates. The effect of temperature on adsorption rates can be analyzed from the values of k_2. As lower values of k_2 favor the adsorption of metal adsorbates and the lowest values of k_2 are observed at minimum temperature, *i.e.*, 25 °C. This confirms that lower temperatures are more suitable for maximum adsorption by MXenes nanosheets. Therefore, a higher temperature than 25 °C is not favorable for the maximum adsorption capacities of $Ti_3C_2T_x$ nanosheets. Moreover, the influence of temperature on adsorption kinetics can be analyzed through equilibrium data. Adsorption equilibrium for Cr(VI) and Pb(II) adsorbates are achieved at 7 min and 4 min of sonication, respectively, as shown in Fig. S5 (ESI†). This implies that only 10 min of sonication at 25 °C is adequately practical to achieve the best adsorption performance. These findings confirm that the adsorption efficiency of $Ti_3C_2T_x$ nanosheets is driven by physiochemical interactions, and the adsorption equilibrium is attained within a few min of sonication.

Table 3 Adsorption isotherms data for Cr(VI) and Pb(II) is presented against Langmuir and Freundlich models

	Langmuir			Freundlich		
HM ion	q_m (mg g^{-1})	K_L	R^2	K_f	$1/n$	R^2
Cr(VI)	5000	0.0024	0.5254	9.54	1.0816	0.9919
Pb(II)	667.67	0.014	0.8227	1.194	1.8720	0.9253

Langmuir and Freundlich isotherms models were applied to analyze the interactions between adsorbates and adsorbents. The linear equations of Langmuir and Freundlich models are given as eqn (5) and (6), respectively.[60] Where C_e and q_e denote the concentration and adsorption capacities at equilibrium, and q_m denotes the adsorption capacity. K_L, K_F and n are the isotherm constants, which represent adsorption energy, adsorption capacity and adsorption intensity, respectively. The Langmuir isotherm is assumed to be applicable for homogenous and monolayer adsorption. Freundlich isotherm can express heterogeneous and multilayer adsorption.[61] The data is presented in Table 3, and their outcome is plotted in Fig. 6.

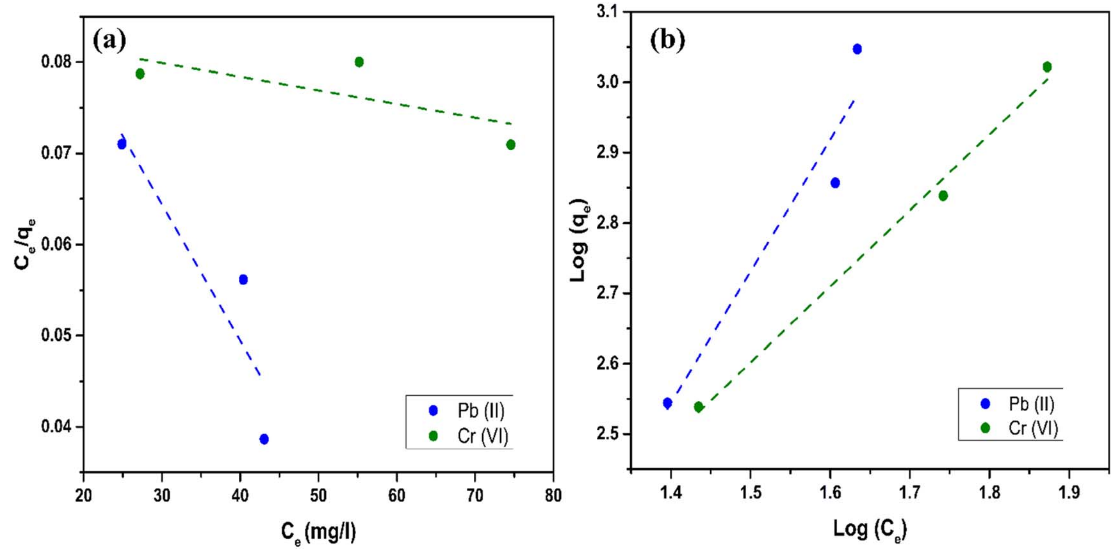

Fig. 6 Adsorption isotherms data for Cr(VI) and Pb(II) is plotted against (a) Langmuir, and (b) Freundlich models.

$$\frac{C_e}{q_e} = \frac{1}{K_L q_m} + \frac{C_e}{q_m} \tag{5}$$

$$\log q_e = \log K_F + \frac{1}{n} \log C_e \tag{6}$$

A plot of C_e/q_e *vs.* C_e is used to determine the constants of the Langmuir model. The Langmuir model represents monolayer adsorption on a uniformed adsorbent's surface with a fixed number of adsorption sites.[62] Likewise, a plot of $\ln C_e$ *vs.* $\ln q_e$ is used to determine the constants of the Freundlich model. Langmuir and Freundlich isotherms parameters were determined from Fig. S6 (ESI) and Fig. S7 (ESI†). The values of R^2 for Freundlich model are higher which implies that the Freundlich model is well-fitted with the experimental data. The values of $1/n$ provide a significant information regarding adsorption of MI. For instance, if it is less than 1, then an ordinary Langmuir isotherm is implied. If $1/n$ value is greater than 1, it indicates cooperative adsorption.[61] The cooperative adsorption occurs due to an interaction between the adsorbate and adsorbent, and also between the adsorbents, which leads to a multilayer adsorption. Here, values of $1/n$ are greater than 1 for MI adsorption, therefore it reflects a multilayered adsorption. This multilayer adsorption further contributes to an enhanced adsorption capacity of $Ti_3C_2T_x$ nanosheets for the MI on the heterogeneous active sites *i.e.*, (–OH) and (–COOH) terminations. Thus, the implication of Freundlich isotherm ensures a heterogeneous adsorption of MI on the MXenes surface. This type of adsorption leads to structural changes in the MXenes nanosheets. The XRD pattern of Cr–$Ti_3C_2T_x$ and Pb–$Ti_3C_2T_x$ nanosheets also shows peak shift towards higher angle, indicating a decrease in the *d*-spacing as discussed in the respective section. The peak shift signifies the effect of heterogenous adsorption on the structure of $Ti_3C_2T_x$ nanosheets.

3.4 Adsorption mechanism

The FTIR and XPS were applied to understand the adsorption mechanism of $Ti_3C_2T_x$ nanosheets. As evident from FTIR spectrums (Fig. 1) that new peaks of Cr_2O_7, $Cr(OH)_3$, and PbO

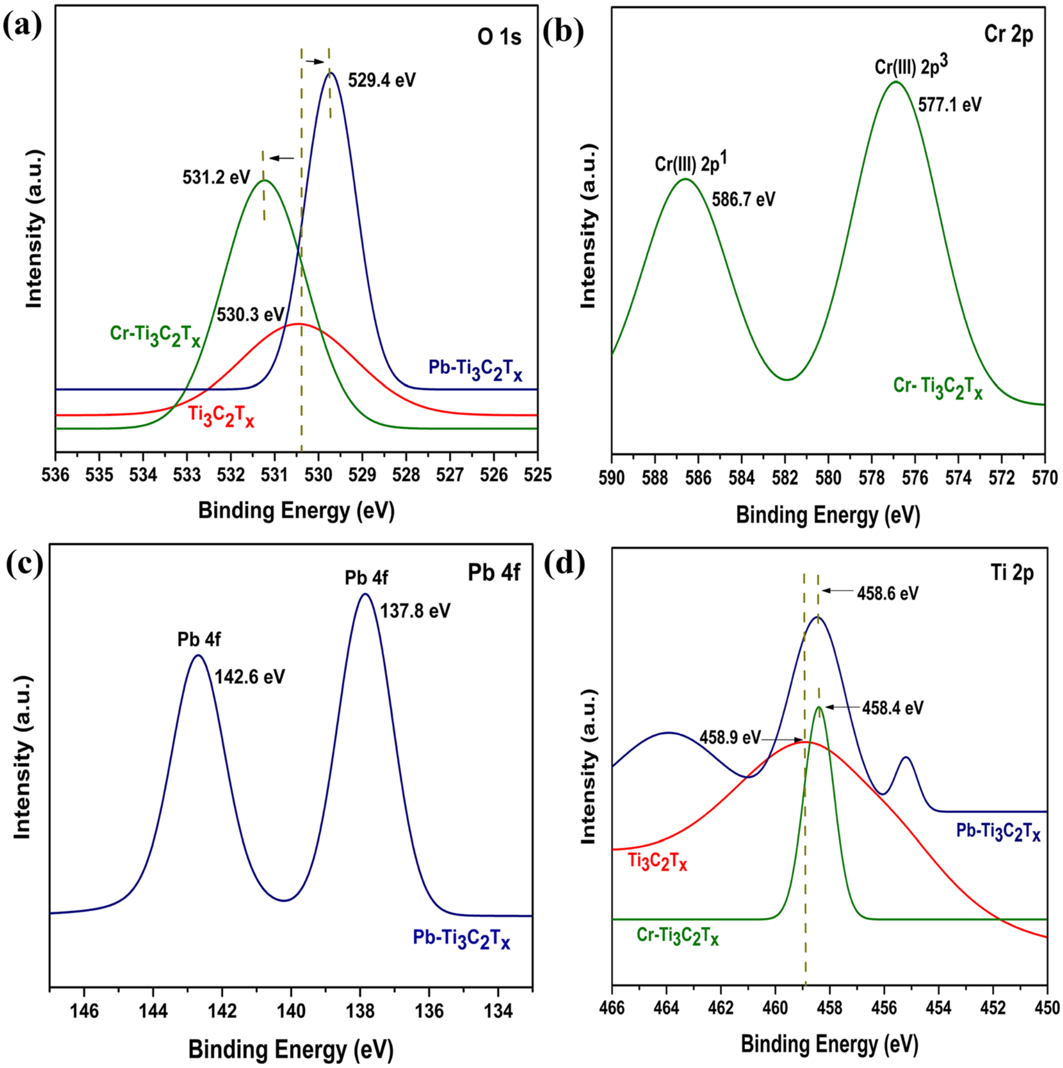

Fig. 7 The XPS spectrums of the bare (in red pattern), Cr(VI) and Pb(II) loaded $Ti_3C_2T_x$ reflected by green and blue patterns, respectively, display the (a) O 1s, (b) Cr 2p, (c) Pb 4f, and (d) Ti 2p bonding states.

emerged due to the uptake of Cr(VI) and Pb(II) by $Ti_3C_2T_x$ nanosheets. Furthermore, slight peaks shifting to lower wave numbers in metal-loaded nanosheets corresponds to C–O and Ti–O bands stretching. These details verify that Cr(VI) is reduced to Cr(III) state to form $Cr(OH)_3$, whereas Pb(II) forms an oxide as PbO during adsorption by $Ti_3C_2T_x$ nanosheets.[63] This further reflects that (–COOH) and (–OH) terminal groups perform a vital role in the adsorption of Cr(VI) and Pb(II) through H^+ exchange. Alongside ion exchange interaction, chemical coordination provided by oxygen (=O) terminal groups come into play for Pb(II) adsorption.[44] Thus, at a time, more active sites are available to Pb(II) than Cr(VI), and that is why $Ti_3C_2T_x$ nanosheets offer more significant and faster adsorption performance for the removal of Pb(II) adsorbates. In addition, the XPS data is also consistent with the above findings. Fig. 7(a) shows the bonding states of $Ti_3C_2T_x$ nanosheets before and after the adsorption of Cr(VI) and Pb(II). A significant shift in the peak intensities after the adsorption of MI can be noticed, which corresponds to an interaction of MI with hydroxyl groups of Ti–OH and O=C–OH terminal functional groups. This further reflects that an ion exchange occurs between the MI and H^+. Furthermore, two peaks in the Cr 2p spectrum, as shown in Fig. 7(b), correspond to the binding energies of 577.1 eV and 586.7 eV. These peaks are attributed to Cr(III) as a result of the reduction of Cr(VI) during the adsorption process.[64] Likewise, two peaks at 137.8 eV and 143.1 eV, as shown in Fig. 7(c), corresponding to the bond state of Pb 4f, which is attributed to the adsorption of Pb(II) through an ion exchange mechanism.[26] However, the lower binding energy of Pb(II) in the O 1s spectrum implies a greater electron density around Pb, possibly due to the chemical coordination between electron donor oxygen and Pb(II). Moreover, a shift in Ti 2p to lower binding energies can be observed after the adsorption of MI, as shown in Fig. 7(d), which confirms a strong chemical interaction between Ti–O and MI.

Hence, multilayered adsorption of Cr(VI) and Pb(II) adsorbates occurs through chemisorption coupled with physisorption reactions. Electrostatic interactions between the positively charged MI and negatively charged terminal groups are found to be the core forces of attraction. In addition to chemisorption *via* ion exchange and coordination interactions, a physisorption through van der Waals forces and entrapment of the MI by the $Ti_3C_2T_x$ nanosheets also enhance the adsorption performance at a lower temperature, mild sonication duration, and higher MI concentration. The overall adsorption mechanism is also schematically presented in Fig. 8.

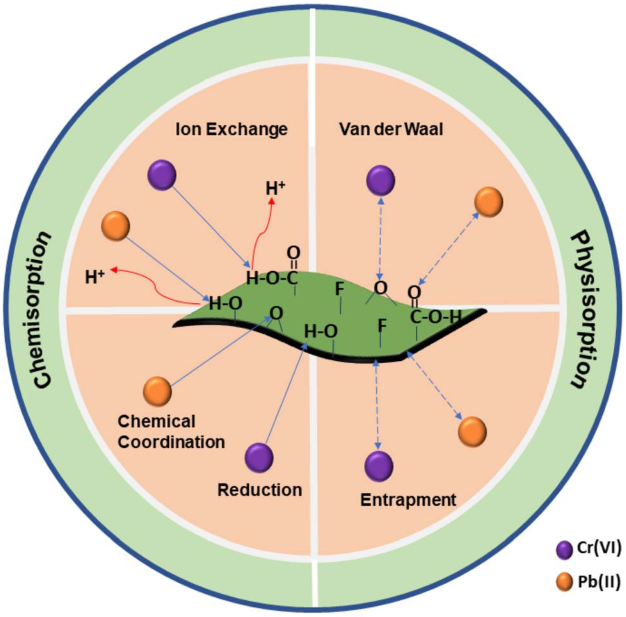

Fig. 8 The adsorption mechanism of $Ti_3C_2T_x$ nanosheets for Cr(VI) and Pb(II) adsorbates depicts the physiochemical interactions between the adsorbent and MI.

3.5 Selectivity and regeneration

The selectivity of $Ti_3C_2T_x$ nanosheets towards Cr(VI) and Pb(II) in a combined feed solution was determined using eqn (7). Adsorption efficiency for Cr(VI) and Pb(II) was found to be 95% and 99%, respectively. Thus, the nanosheets adsorbent displayed superior and preferable adsorption for Pb(II) as the electronegativity of Pb is 1.87, which is greater than 1.66 of Cr metal. This also verifies that the interactions of Pb(II) and Cr(VI) adsorbates with the nanosheets adsorbent occur mainly through electrostatic forces. Similarly, the selectivity of the nanosheets towards toxic Cr(VI) and Pb(II) pollutants in presence of Ca(II), Na(II) and K(I) competing ions was evaluated. The adsorption efficiency of the nanosheets for each cation was determined and plotted as shown in Fig. 9(a). The competing cations lead to a reduction in the adsorption performance for Cr(VI) and Pb(II) in the order as Ca(II) > Na(II) > K(I) with electronegativity of 1 > 0.93 > 0.82, respectively. This reflects the effect on the adsorption of the nanosheets is related to the electronegative of the adsorbate ions. Thus, more electronegative co-ions affect the adsorption efficiency with greater intensity.

$$\text{Selectivity} = \frac{100 - E(\text{Pb})}{100 - E(\text{Cr})} \tag{7}$$

where E refers to the adsorption efficiencies of the Pb(II) and Cr(VI) MI.

The regeneration and reusability of the $Ti_3C_2T_x$ nanosheets regarding Cr(VI) and Pb(II) removal were also evaluated. The MXenes slurry obtained through vacuum filtration after the first adsorption cycle was sonicated in 150 mL solution of 0.1 M NaOH (concentration of 4 g of NaOH in 1000 mL DI water) at 30 kHz for 6 h. Thus, the MXenes adsorbent was regenerated over six adsorption–desorption cycles, and its efficiency was recorded and plotted, as shown in Fig. 9(b). This indicates that $Ti_3C_2T_x$ nanosheets adsorbent has an excellent regeneration and reusability tendency, and even after six cycles, its efficiency remains 80% and 97% for Cr(VI) and Pb(II), respectively. This further reflects that after adsorption–desorption cycles, the nanosheets retain their SSA and terminal functional groups quite effectively. Hence, these nanosheets can efficiently be applied to eliminate other metal contaminants from an aqueous environment.

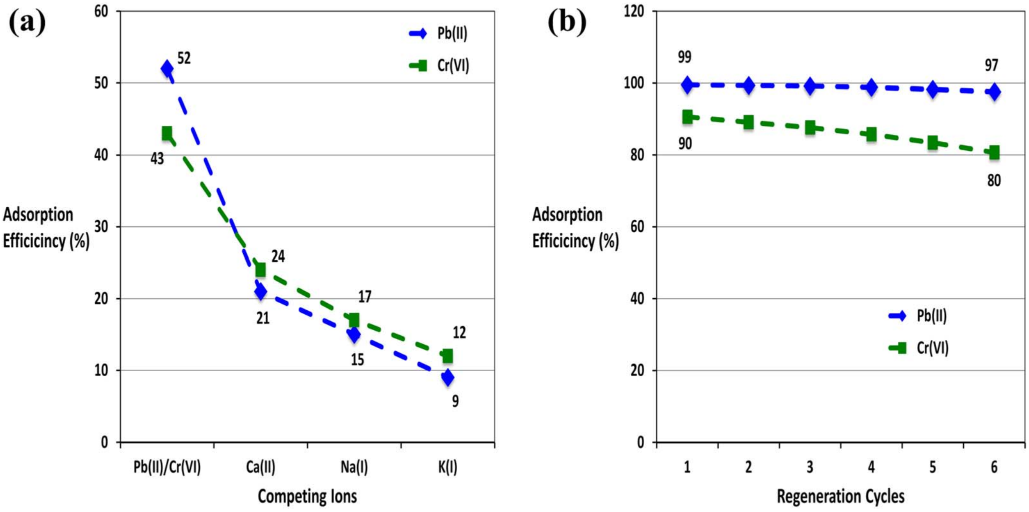

Fig. 9 The adsorption efficiency of $Ti_3C_2T_x$ nanosheets for Cr(VI) and Pb(II) (a) in the presence of competing cations, and (b) over six cycles of regeneration and reusability.

4. Conclusion

In this study, carboxylic terminated $Ti_3C_2T_x$ nanosheets were successfully synthesized and applied for the removal of toxic Cr(VI) and Pb(II) pollutants from an aqueous media. The nanosheets displayed extraordinary adsorption capacities of 1090 mg g^{-1} and 1135 mg g^{-1} for Cr(VI) and Pb(II), respectively, and achieved adsorption equilibrium very rapidly. The best adsorption capacity was attained at 30 kHz sonication for 10 min duration, 600 ppm of MI concentration, and 25 °C temperature of the solution at pH 5.5. Moreover, the kinetic and isotherm studies of the nanosheets reflected a physiochemical adsorption process. The (–COOH) and (–OH) terminals played a vital role in the enhanced and rapid uptake of Cr(VI) and Pb(II) contaminants through an ion exchange mechanism. Other interactions including, chemical coordination, entrapment, and van der Waal forces, also contributed to the adsorption of MI adsorbates. In addition, $Ti_3C_2T_x$ nanosheets showed a better selectivity towards Pb(II) removal than Cr(VI) as well other competing cations. However, those cations also adversely affected the adsorption performance for Cr(VI) and Pb(II) in the order of Ca(II) > Na(II) > K(I). Furthermore, over six cycles of regeneration and reusability, the nanosheets displayed adsorption efficiencies of 80% for Cr(VI) and 90% for Pb(II), which was quite economical and encouraging. Basing on the efficient adsorption performance for Cr(VI) and Pb(II) pollutants, and in comparison to the previously reported titanium carbide and activated carbon-based adsorbents, these high-quality $Ti_3C_2T_x$ nanosheets may be applied for the elimination of other hazardous MI contaminants from the aquatic environment.

Author contributions

Saleem Shah: conceptualization, experimentation, analysis, writing. Iqra Mubeen: coordination, graphs and images plotting. Erum Pervaiz: supervision, provision of materials. Habib Nasir: reviewing, mentoring.

Conflicts of interest

We affirm no conflict of interest.

Acknowledgements

We recognize the assistance provided by SCME, NUST, Islamabad, Pakistan. We would also thank NUST authorities for providing characterization and testing facilities.

References

1 J. Briffa, E. Sinagra and R. Blundell, *Heliyon*, 2020, **6**, e04691.
2 J. Lubchenco, *Science*, 1998, **279**, 491–497.
3 H. A. T. Banu, P. Karthikeyan, S. Vigneshwaran and S. Meenakshi, *Int. J. Biol. Macromol.*, 2020, **154**, 188–197.
4 M. Balali-Mood, K. Naseri, Z. Tahergorabi, M. R. Khazdair and M. Sadeghi, *Front. Pharmacol.*, 2021, 227.
5 H. J. Gibb, P. S. Lees, P. F. Pinsky and B. C. Rooney, *Am J. Ind. Med.*, 2000, **38**, 115–126.
6 P. Apostoli, A. Bellini, S. Porru and L. Bisanti, *Am. J. Ind. Med.*, 2000, **38**, 310–315.
7 C. S. Chetty, G. R. Reddy, K. S. Murthy, J. Johnson, K. Sajwan and D. Desaiah, *Int. J. Toxicol.*, 2001, **20**, 113–120.
8 L. Joseph, B.-M. Jun, J. R. V. Flora, C. M. Park and Y. Yoon, *Chemosphere*, 2019, **229**, 142–159.
9 T. A. Saleh, *Environ. Technol. Innov.*, 2021, **24**, 101821.
10 A. R. Karbassi and S. Nadjafpour, *Environ. Pollut.*, 1996, **93**, 257–260.
11 R. Davarnejad and P. Panahi, *Sep. Purif. Technol.*, 2016, **158**, 286–292.

12 Y.-C. Lai, Y.-R. Chang, M.-L. Chen, Y.-K. Lo, J.-Y. Lai and D.-J. Lee, *Bioresour. Technol.*, 2016, **214**, 192–198.

13 R. Lertlapwasin, N. Bhawawet, A. Imyim and S. Fuangswasdi, *Sep. Purif. Technol.*, 2010, **72**, 70–76.

14 S. Mauchauffée and E. Meux, *Chemosphere*, 2007, **69**, 763–768.

15 B. Rahmanian, M. Pakizeh, M. Esfandyari, F. Heshmatnezhad and A. Maskooki, *J. Hazard Mater.*, 2011, **192**, 585–592.

16 A. S. Dharnaik and P. K. Ghosh, *Environ. Technol.*, 2014, **35**, 2272–2279.

17 J. Yoon, G. Amy, J. Chung, J. Sohn and Y. Yoon, *Chemosphere*, 2009, **77**, 228–235.

18 R. Guillossou, J. Le Roux, R. Mailler, C. S. Pereira-Derome, G. Varrault, A. Bressy, E. Vulliet, C. Morlay, F. Nauleau and V. Rocher, *Water Res.*, 2020, **172**, 115487.

19 M. Wang, W. Cheng, T. Wan, B. Hu, Y. Zhu, X. Song and Y. Sun, *Chem. Eng. J.*, 2019, **362**, 99–106.

20 L. Niazi, A. Lashanizadegan and H. Sharififard, *J. Clean. Prod.*, 2018, **185**, 554–561.

21 Y. Yang, J. Yang, Y. Du, C. Li, K. Wei, J. Lu, W. Chen and L. Yang, *ACS Omega*, 2019, **4**, 17741–17751.

22 R. Fu, Y. Yang, Z. Xu, X. Zhang, X. Guo and D. Bi, *Chemosphere*, 2015, **138**, 726–734.

23 C. H. Weng, J. H. Wang and C. P. Huang, *Water Sci. Technol.*, 1997, **35**, 55–62.

24 B.-M. Jun, S. Kim, Y. Kim, N. Her, J. Heo, J. Han, M. Jang, C. M. Park and Y. Yoon, *Chemosphere*, 2019, **231**, 82–92.

25 Y. Ying, Y. Liu, X. Wang, Y. Mao, W. Cao, P. Hu and X. Peng, *ACS Appl. Mater. Interfaces*, 2015, **7**, 1795–1803.

26 B.-M. Jun, N. Her, C. M. Park and Y. Yoon, *Environ. Sci.*, 2020, **6**, 173–180.

27 H. Wang, F. Wu, Z. Wang, Y. Wang, S. Zhang, H. Luo, Z. Zheng and L. Fang, *Chemosphere*, 2022, **308**, 136573.

28 Y. Lv, K. Chang, H. Wu, P. Fang, C. Chen and Q. Liao, *Water Sci. Technol.*, 2021, **84**, 2446–2456.

29 Y. Du, B. Yu, L. Wei, Y. Wang, X. Zhang and S. Ye, *J. Mater. Sci.*, 2019, **54**, 13283–13297.

30 A. S. Jatoi, N. M. Mubarak, Z. Hashmi, N. H. Solangi, R. R. Karri, T. Y. Hua, S. A. Mazari, J. R. Koduru and A. Alfantazi, *Chemosphere*, 2022, 137497.

31 S. Wang, Y. Liu, Q.-F. Lü and H. Zhuang, *J. Mol. Liq.*, 2020, **297**, 111810.

32 Y. Ying, Y. Liu, X. Wang, Y. Mao, W. Cao, P. Hu and X. Peng, *ACS Appl. Mater. Interfaces*, 2015, **7**, 1795–1803.

33 P. Karthikeyan, K. Ramkumar, K. Pandi, A. Fayyaz, S. Meenakshi and C. M. Park, *Ceram. Int.*, 2021, **47**, 3692–3698.

34 H. Wang, H. Cui, X. Song, R. Xu, N. Wei, J. Tian and H. Niu, *J. Colloid Interface Sci.*, 2020, **561**, 46–57.

35 Q. Peng, J. Guo, Q. Zhang, J. Xiang, B. Liu, A. Zhou, R. Liu and Y. Tian, *J. Am. Chem. Soc.*, 2014, **136**, 4113–4116.

36 S. Wang, Y. Liu, Q.-F. Lü and H. Zhuang, *J. Mol. Liq.*, 2020, **297**, 111810.

37 M. Li, J. Lu, K. Luo, Y. Li, K. Chang, K. Chen, J. Zhou, J. Rosen, L. Hultman and P. Eklund, *J. Am. Chem. Soc.*, 2019, **141**, 4730–4737.

38 Y. Huang and Z. Wang, *Int. J. Biol. Macromol.*, 2018, **107**, 741–747.

39 L. M. Alrehaily, J. M. Joseph, A. Y. Musa, D. A. Guzonas and J. C. Wren, *Phys. Chem. Chem. Phys.*, 2013, **15**, 98–107.

40 S. Myhra, J. A. A. Crossley and M. W. Barsoum, *J. Phys. Chem. Solids*, 2001, **62**, 811–817.

41 M. Naguib, O. Mashtalir, J. Carle, V. Presser, J. Lu, L. Hultman, Y. Gogotsi and M. W. Barsoum, *ACS Nano*, 2012, **6**, 1322–1331.

42 A. Kubacka, B. Bachiller-Baeza, G. Colón and M. Fernández-García, *Appl. Catal. B Environ.*, 2010, **93**, 274–281.

43 G. Zhang, T. Wang, Z. Xu, M. Liu, C. Shen and Q. Meng, *Chem. Commun.*, 2020, **56**, 11283–11286.

44 Y. Dong, D. Sang, C. He, X. Sheng and L. Lei, *RSC Adv.*, 2019, **9**, 29015–29022.

45 P. Gu, S. Zhang, C. Zhang, X. Wang, A. Khan, T. Wen, B. Hu, A. Alsaedi, T. Hayat and X. Wang, *Dalton Trans.*, 2019, **48**, 2100–2107.

46 Z. Zhang, T. Wang, H. Zhang, Y. Liu and B. Xing, *Sci. Total Environ.*, 2021, **757**, 143910.

47 O. A. A. Eletta, F. O. Ayandele and J. O. Ighalo, *Biomass Convers. Biorefin.*, 2021, **13**, 9831–9840.

48 A. Kong, Y. Sun, M. Peng, H. Gu, Y. Fu, J. Zhang and W. Li, *Colloids Surf. A Physicochem. Eng. Asp.*, 2021, **617**, 126388.

49 Y. Feng, H. Wang, J. Xu, X. Du, X. Cheng, Z. Du and H. Wang, *J. Hazard Mater.*, 2021, **416**, 125777.

50 L. He, D. Huang, Z. He, X. Yang, G. Yue, J. Zhu, D. Astruc and P. Zhao, *J. Hazard Mater.*, 2020, **388**, 121761.

51 L. Jin, L. Chai, W. Yang, H. Wang and L. Zhang, *Int. J. Environ. Res. Publ. Health*, 2020, **17**, 167.

52 A. R. Khan, S. K. Awan, S. M. Husnain, N. Abbas, D. H. Anjum, N. Abbas, M. Benaissa, C. R. Mirza, S. Mujtaba-ul-Hassan and F. Shahzad, *Ceram. Int.*, 2021, **47**, 25951–25958.

53 Y. Tang, C. Yang and W. Que, *J. Adv. Dielectric.*, 2018, **8**, 1850035.

54 X. Xie, C. Chen, N. Zhang, Z.-R. Tang, J. Jiang and Y.-J. Xu, *Nat. Sustain.*, 2019, **2**, 856–862.

55 G. Zou, J. Guo, Q. Peng, A. Zhou, Q. Zhang and B. Liu, *J. Mater. Chem. A*, 2016, **4**, 489–499.

56 M. Jain, M. Yadav, T. Kohout, M. Lahtinen, V. K. Garg and M. Sillanpää, *Water Resour. Ind.*, 2018, **20**, 54–74.

57 J. Kaur, M. Kaur, M. K. Ubhi, N. Kaur and J.-M. Greneche, *Mater. Chem. Phys.*, 2021, **258**, 124002.

58 C. M. Park, Y. A. J. Al-Hamadani, J. Heo, N. Her, K. H. Chu, M. Jang, S. Lee and Y. Yoon, *Ultrason. Sonochem.*, 2017, **39**, 750–757.

59 H. K. Agbovi and L. D. Wilson, in *Natural polymers-based green adsorbents for water treatment*, Elsevier, 2021, pp. 1–51.

60 J. López-Luna, L. E. Ramírez-Montes, S. Martinez-Vargas, A. I. Martínez, O. F. Mijangos-Ricardez, M. d. C. A. González-Chávez, R. Carrillo-González, F. A. Solís-Domínguez, M. d. C. Cuevas-Díaz and V. Vázquez-Hipólito, *SN Appl. Sci.*, 2019, **1**, 1–19.

61 T. R. Sahoo and B. Prelot, in *Nanomaterials for the Detection and Removal of Wastewater Pollutants*, ed. B. Bonelli, F. S.

Freyria, I. Rossetti and R. Sethi, Elsevier, 2020, pp. 161–222, DOI: 10.1016/B978-0-12-818489-9.00007-4.

62 I. H. Ali, M. K. Al Mesfer, M. I. Khan, M. Danish and M. M. Alghamdi, *Processes*, 2019, **7**, 217.

63 S. M. Prabhu, K. Pandi, S. S. Elanchezhiyan, J.-y. Choi, G. P. Kalaignan and C. M. Park, *Sep. Purif. Technol.*, 2020, **235**, 116247.

64 X. Guo, G. T. Fei, H. Su and L. De Zhang, *J. Phys. Chem. C*, 2011, **115**, 1608–1613.